







FULL ARTICLE

Optical windows for head tissues in near-infrared and short-wave infrared regions: Approaching transcranial light applications

Sergii Golovynskyi¹  | Iuliia Golovynska¹  | Ludmila I. Stepanova²  | Oleksandr I. Datsenko³  |
Liwei Liu¹ | Junle Qu^{1*}  | Tymish Y. Ohulchanskyy^{1*} 

¹Key Laboratory of Optoelectronic Devices and Systems of Ministry of Education and Guangdong Province, College of Optoelectronic Engineering, Shenzhen University, Shenzhen, China

²Institute of Biology and Medicine, Taras Shevchenko National University of Kyiv, Kyiv, Ukraine

³Physics Faculty, Taras Shevchenko National University of Kyiv, Kyiv, Ukraine

***Correspondence**

Junle Qu, Key Laboratory of Optoelectronic Devices and Systems of Ministry of Education and Guangdong Province, College of Optoelectronic Engineering, Shenzhen University, Shenzhen, 518060, China.

Email: jlqu@szu.edu.cn

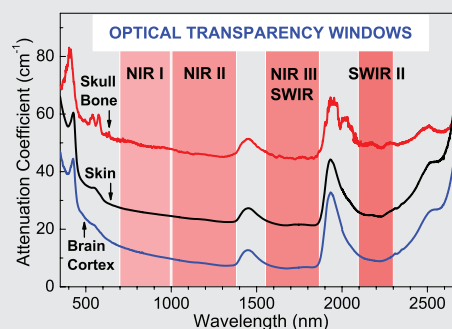
Tymish Y. Ohulchanskyy, Key Laboratory of Optoelectronic Devices and Systems of Ministry of Education and Guangdong Province, College of Optoelectronic Engineering, Shenzhen University, Shenzhen, 518060, China.

Email: tyo@szu.edu.cn

Funding information

Guangdong Natural Science Foundation Innovation Team, Grant/Award Number: 2014A030312008; National Basic Research Program of China, Grant/Award Number: 2015CB352005; National Natural Science Foundation of China, Grant/Award Number: 61525503, 61620106016, 81727804, 61722508; Shenzhen Basic Research Project, Grant/Award Number: JCYJ20150930104948169, JCYJ20160328144746940, GJHZ20160226202139185, JCYJ20170412105003520

Optical properties of the rat head tissues (brain cortex, cranial bone and scalp skin) are assessed, aiming at transcranial light applications such as optical imaging and phototherapy. The spectral measurements are carried out over the wide spectral range of 350 to 2800 nm, involving visible, near-infrared (NIR) and short-wave infrared (SWIR) regions. Four tissue transparency windows are considered: ~700 to 1000 nm (NIR-I), ~1000 to 1350 nm (NIR-II), ~1550 to 1870 nm (NIR-III or SWIR) and ~2100 to 2300 nm (SWIR-II). The values of attenuation coefficient and total attenuation length are determined for all windows and tissue types. The spectra indicate transmittance peaks in NIR, NIR-II and SWIR-II, with maximum tissue permeability for SWIR light. The use of SWIR-II window for the transcranial light applications is substantiated. Furthermore, absorbance of the head tissues is investigated in details, by defining and describing the characteristic absorption peaks in NIR-SWIR.



KEYWORDS

attenuation, bone, brain, optical tissue window, short-wave infrared, skin, skull, transcranial imaging

1 | INTRODUCTION

Biophotonics, involving interaction of light and biomaterials, is among the most promising and actively developing multidisciplinary approaches expected to make a major impact on health care [1–5]. The ability of light to penetrate

into tissue is a key for diagnostic (eg, optical bioimaging) and therapeutic (eg, light induced therapy and drug delivery) applications of biophotonics.

The main advantage of optical imaging is high spatial resolution (ie, submicron range) that cannot be achieved by other bioimaging techniques, such as magnetic resonance imaging (MRI), X-ray and ultrasound imaging. On the other hand, a major drawback for optical imaging is associated

Sergii Golovynskyi and Iuliia Golovynska contributed equally to this study.

with optical properties of biological tissues, which results in a limited light penetration. The penetration of light in visible and the shortest near-infrared (NIR-I) ranges of electromagnetic spectrum (ie, 400–700 and ~700–1000 nm, respectively) is well characterized for most biological matters [5–12] including head [13–17] and brain [17–21]. NIR light has been found to better propagate through tissue than the visible one, and, in the beginning of 1980th, NIR-I region has been introduced by Parrish and Anderson as the diagnostic or therapeutic window [6, 7]. Over the last decades, the optical tissue transparency window in NIR-I has been employed for noninvasive optical bioimaging of small animals in biomedical research [22–28], advancing the development of imaging guided phototherapy and drug delivery [29]. Quite recently, in addition to the conventional NIR-I window, two or more optical windows have been identified, namely NIR-II (~1000–1350 nm) [30–32] and NIR-III or short-wave IR (SWIR) (~1550–1870 nm) [31–36].

Being encouraged by a rapid progress in the development of new NIR-SWIR sensitive cameras based on InGaAs or InSb photodetectors and new laser sources [30, 37–40], the use of NIR-SWIR light for in vivo applications (ie, optical imaging and therapy) are being actively advanced. These windows allow researchers to benefit from the reduced tissue scattering and autofluorescence in these spectral regions and achieve deeper light penetration [23, 24]. In particular, NIR-I and NIR-II windows have been shown to be suitable for the through-skull brain imaging in vivo [22–25]. Moreover, few recent studies have found that light in SWIR (or NIR-III) window has even better tissue permeability [31–36], that makes it advantageous for the imaging utilizing exogenous and endogenous agents [41–43].

The use of the fourth window at ~2100 to 2300 nm has recently been suggested for soft tissues, such as skin [6–8], muscle [11], adipose [9, 11, 16] and internal organs [11, 32, 44], and also for brain in the recent study by Shi et al. [18]. Therein, this spectral window centered at 2200 nm has been termed as NIR-IV window [18]. In the current article, we term it as SWIR-II, since SWIR is used more frequently in recent years [33, 35, 36], apparently due to a rapid progress in the development of the SWIR detectors [37, 45]. SWIR-II window demonstrate a promising potential for brain imaging in comparison with NIR-II one in terms of collimated/ballistic light permeability [16, 18]. It was shown for skin and other soft tissues that light attenuation in SWIR-II region is comparable with that in NIR-I one, where tissues exhibit higher scattering [6–11].

Herein, we present our study of absorption and scattering properties of various head tissue types, such as brain cortex, skin scalp and cranial bone freshly harvested from rats. An investigation of the tissue optical properties was performed in the broad spectral range from visible to NIR and to SWIR (350–2800 nm); the spectra of attenuation coefficient and total attenuation length have been obtained for all optical

transparency windows, as the first step toward a proper design of the optical bioimaging method. The tissue permeability (collimated transmittance as well as resulted attenuation and attenuation depth) was also determined.

We have shown that light in SWIR-II window, centered at 2200 nm, has a moderate attenuation by skull bone and other head tissues and appears promising for the transcranial light applications (eg, brain imaging or phototherapy). It should be noted that the spectra of bone NIR light permeability have mostly been reported for a narrow spectral range, with only mentioning of the increase in light penetration toward IR range [13]. The fundamental works [14, 16] is the only two, where the optical parameters of human cranial bone have been characterized in a rather broad spectral range (~650–2500 nm), showing that bone permeability is similar to biological turbid medium, with a high absorption in SWIR. In our work, we extended the spectral range, where the head tissues were investigated in-details, covering the range from 350 to 2800 nm. Such an approach is of importance thanks to the development of new detection techniques and detectors with sensitivity extended toward NIR-SWIR range [30, 37]; the reduced scattering and absence of autofluorescence in SWIR-I, II windows can provide major benefits for optical bioimaging. We have analyzed the disparities in light extinction for the freshly collected animal head tissues (ie, skin, cranial bone and brain) and investigated the characteristic absorption bands of the brain, skin and bone constituents in the range from NIR-II to SWIR-II, which can be of use for the development of optical imaging with endogenous contrast agents. Based on the obtained results, the possibility to utilize the SWIR-I, II light for the in vivo transcranial applications has been assessed.

2 | MATERIALS AND METHODS

2.1 | Specimen preparation

Fresh albino rat tissues were used for all experiments, which were performed in strict accordance with the recommendations about the general ethical principles of animal experiments of “Guide for the Care and Use of Laboratory Animals” by the National Institutes of Health. Five mature 4- to 5-month-old healthy male rats weighing 180 to 200 g were maintained in collective cages under standard controlled conditions on a 12 hour light/dark cycle and fed standard rodent chow and water ad libitum. The animals were anesthetized with urethane (Sigma-Aldrich, St. Louis, Missouri) injected intraperitoneally (1.1 g kg^{-1}), and thereafter sacrificed via urethane overdose (3 g kg^{-1}). The fur was removed from the head, and an incision was made, which permitted the brain to be removed individually. A full thickness skin from the head and forehead cranial bone were excised in the $1.3 \times 1.3 \text{ cm}$ square samples. One set of samples was extracted from each animal of five.

The postmortem tissue samples were rinsed in saline to remove excessive blood and then dissected using scalpel and sliced at a thickness of 1 mm using a vibration microtome. The brain slices were taken from the cortex, so the samples mostly consisted of the gray matter. The skin and brain samples were placed between two microscope glass slides with 1 mm spacers, determining the sample thickness and protecting it from air drying. As the samples were previously accurately sliced to be 1 mm, the tissue compression was insignificant. Then, the slides were mounted in a sample holder. The head tissue extraction and sample preparation are schematically illustrated in Figure 1A. The net thickness of skull bone was determined by micrometer measurements as 0.9 mm. The specimen edges were not involved in the optical measurements, whereas the central area was exposed to the light beam. Spectral measurements with the as-prepared tissue samples started at ~1 hour after extraction.

After the optical measurements, the samples inside a covered Petri dish were placed on a heating plate with temperature of 36°C and dried for 20 days, to be then measured in a desiccated state. The average residual humidity of samples was 14%, as determined by a humidity meter. The desiccated samples did not show any signs of biodegradation.

2.2 | Transmission and absorption measurements

The total transmission, scattered transmission and diffuse reflectance (back scattering) spectra were measured using a spectrophotometer Shimadzu UV-3600 (Shimadzu, Kyoto, Japan) equipped with an integrating sphere. Using the standard protocols [8, 20], three types of measurement configurations in the sphere were performed for each sample. A scheme of measurements in different operating modes is given in Figure 1C. If the prepared slide was placed in front of the sphere at the scatter transmission port (left picture), the diffusely transmitted or forward-scattered light was collected; in the other mode, placing the slide in the reflectance port in backside of the sphere (right picture), the light diffusely reflected by a turbid biological media was detected. Barium sulfate plates were used at the measurements as reflectance standards, using the barium sulfate plate reflectance spectra available in the sphere manual.

First, the total diffused transmittance T_d was measured with a reflectance standard at the reflectance port; T_d is the sum of forward-scattered (T_s) and on-axis collimated transmittance (T_c) as shown in Figure 1B. For example, $T_c = I_c/I_0$, where I_0 and I_c are the intensities of the incident light and light

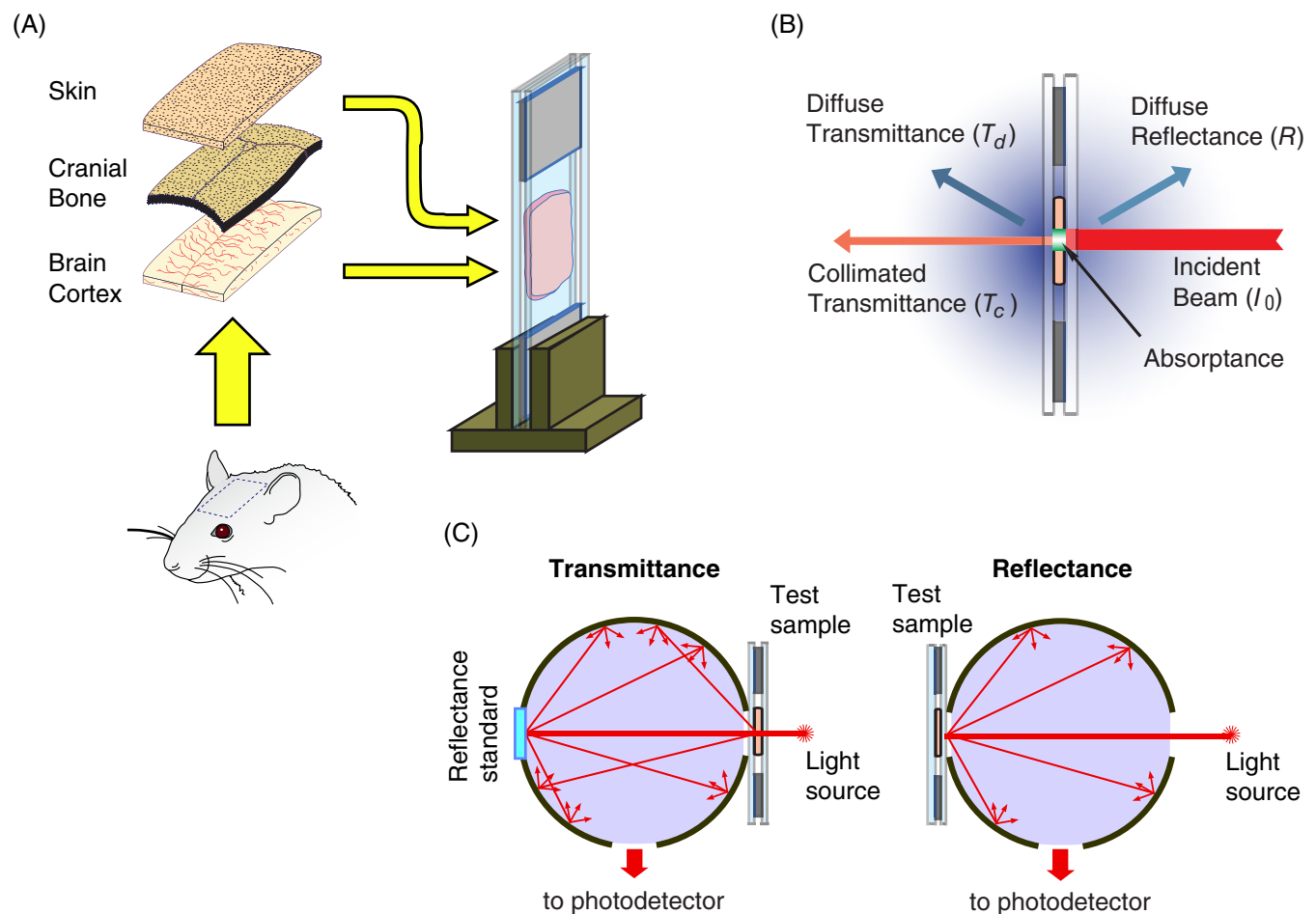


FIGURE 1 (A) Illustrations of the head tissues extraction and slides preparation with soft tissue samples; (B) directionality of the diffusely transmitted and back scattered (diffusely reflected) light as well as collimated path through a flat tissue sample in the prepared slide; (C) scheme of measurements using an integrating sphere in different operating modes

after on-axis collimated path, respectively. Second, T_s was measured with a free reflectance port, that allowed us to calculate the on-axis collimated transmittance as $T_c = T_d - T_s$. However, due to the small dimension of the sphere and the solid angle due to the relatively large dimension of the port, a nonnegligible part of the scattered light will also escape from this open port, resulting in an underestimation of T_s . Because of this, as a correction procedure, we also assessed T_c using the spectrophotometer without the integrating sphere and with a small aperture of 3×3 mm. We found that the acquired T_c values were slightly ($\sim 10\%$) less in case of direct measurements than with integrating sphere. The corresponding correction factor (~ 0.9) was introduced to correct T_c values obtained in the integrating sphere measurements.

Then, the samples were placed on the opposite side of the sphere at the diffuse reflectance port (Figure 1C, right part). In such a geometry, the diffusely reflected or back-scattered part of light (diffuse reflectance R) was collected by photodetector. A part of the light energy absorbed by the sample (absorptance, A) can be determined using T_d and R , considering that $1 = T_d + R + A$, hence $A = 1 - T_d - R$. This part of the light energy is depicted in Figure 1B by green color in the sample.

In the measurements described above, almost all the scattered light from the sample was collected and parameters T_d , T_s and R were obtained. However, a certain part of the light would escape the detector through the sample boundaries, thus increasing the value of measured absorptance of the samples. This aspect was taken into consideration when calculating optical coefficients as described in section 2.3. Moreover, since the fresh samples were placed between two microscopy slides, as shown in Figure 1B, the measurements were also corrected for Fresnel reflection, which originates from the air/glass/water and glass/air interfaces. With this aim, zero reflectance was measured with two empty slides wet inside in the sample beam.

2.3 | Theory

For the collimated path (ballistic photons) in the simplest case of low-scattering media, spectral dependences of the total attenuation coefficient $\mu_t(\lambda)$ and total attenuation length $l_t = 1/\mu_t$ can be obtained from the Beer-Lambert law:

$$T_c(\lambda) = I_c/I_0 = \exp(-\mu_t(\lambda) \cdot d) = \exp(-d/l_t(\lambda)), \quad (1)$$

where d is the light path length (equal to tissue sample thickness), considering that the total attenuation coefficient of a volume is the sum of the absorption and scattering coefficients: $\mu_t = \mu_a + \mu_s$.

Light propagation in biological tissues can be described in terms of radiation transport in a random inhomogeneous turbid media. However, the Beer-Lambert law assumes that the incident light traverses the medium without multiple scattering and that the absorbing moiety is homogeneously distributed along the light path, and, evidently, cannot be

used for calculation of true coefficients in the case of thick biological tissue. Light path through a tissue turbid medium undergoes multiple scattering, resulting in multiple absorption [22].

The theory has been developed with an assumption that multiple light scattering in turbid medium splits the traversed light into coherent (ballistic) and diffusive components [46–48]. The solution to the diffusion equation, which considers both ballistic and diffusive modes, can be presented [18] as

$$T_c(\lambda) = \exp(-\mu_t(\lambda) \cdot d) + \frac{\Omega}{4\pi} \exp(-\mu_{\text{eff}}(\lambda) \cdot d), \quad (2)$$

where Ω is the solid angle, which for thin samples is small, ordered as $\sim 10^{-2}$.

The effective extinction coefficient related to the scattering (diffusive mode) is determined as

$$\mu_{\text{eff}}(\lambda) = \frac{1}{\delta(\lambda)} = \sqrt{3\mu_a[\mu_a + \mu_s(1-g)]} = \sqrt{3\mu_a(\mu_a + \mu'_s)}, \quad (3)$$

where δ is the effective depth of light penetration into biological tissue; and $\mu'_s = \mu_s(1-g)$ represents the reduced scattering coefficient, and $g = \cos(\theta)$ is the anisotropy angular factor, which is wavelength-dependent and varies from 0.7 to 0.98 for most biological tissues, θ denotes the difference between the incident angle and the direction after the scattering event [8, 49].

In tissues where optical scattering is an influential factor, the path length d becomes the total distance traveled by a photon moving through the sample termed the mean path length L . The modified Beer-Lambert law is the empirical expression for a light attenuation in a highly scattering medium [50–52], for transmittance it can be presented [11, 52] as

$$T_c(\lambda) = x_1 \cdot \exp(-\mu_t(\lambda) \cdot L(\lambda) \cdot x_2). \quad (4)$$

Here, two wavelength-independent correction factors were introduced to fit the experimentally observed transmittance (real μ_t is a bit smaller than that obtained from the non-modified Beer-Lambert law). The correction coefficient x_1 is the measurement geometry factor to consider multiply scattered but not absorbed photons, which escape at the sample boundaries thus increasing the apparent absorption. For relatively thin samples (~ 1 mm), factor x_1 varies in the ranges of 0.9 to 0.99 [52]. Although, this is smaller than the disparities in the transmittance measurements, which can reach 40% as a result of 30-minute delay of the ex vivo experiment [11]. The correction coefficient x_2 is the differential path-length factor (a number greater than 1) that compensates increase in the real path length L with the sample effective thickness d caused by the nonstraight light path through the turbid sample.

Nevertheless, for thin samples where the ballistic light component is essential in transmittance, μ_t can be calculated

from the modified Beer-Lambert law using the experimentally observed collimated transmittance T_c , as shown in refs. [11, 18].

$$T_c(\lambda) = x_1 \cdot \exp(-\mu_t(\lambda) \cdot d) = x_1 \cdot \exp(-d/l_t(\lambda)). \quad (5)$$

Thereby, the results of integrating sphere measurements were utilized by us to determine optical coefficients of the samples. First, μ_t spectra can be obtained using

$$\mu_t(\lambda) = \mu_a(\lambda) + \mu_s(\lambda) = \frac{-\ln(T_c/x_1)}{d}. \quad (6)$$

The absorption coefficient μ_a was determined using the well-known one-dimensional two-flux Kubelka-Munk (KM) photon transport theory. KM assumes isotropic scattering and approximates the light transport equation, being somewhat inaccurate when defining optical coefficients [53]. However, KM is still widely recognized as an adequate theory to describe light propagation in turbid biological tissues, as the basic condition for KM applicability, $\mu_a/\mu_s \ll 1$, is fulfilled in most of VIS-NIR range [54–56]. KM provides rather simple mathematical formulations to extract the optical parameters from the experimentally derived T_d , R and d . The KM coefficients A_{KM} and S_{KM} are determined as,

$$A_{KM} = (x-1)S_{KM}, S_{KM} = \frac{1}{y \cdot d} \cdot \ln \left[\frac{1-R(x-y)}{T_d} \right], \quad (7)$$

$$x = \frac{1+R^2-T_d^2}{2R}, y = \sqrt{x^2-1}. \quad (8)$$

The following equations can be used to convert the KM coefficients to μ_a , and μ_s' :

$$A_{KM} = 2\mu_a, S_{KM} = \frac{3}{4}\mu_s'. \quad (9)$$

Spectral dependences of μ_s were determined to fitting the experimental spectra $\mu_s = \mu_t - \mu_a$ within the scattering theory, assuming that Mie scattering makes the major contribution in the long-wavelength range [8, 9, 14], while Rayleigh scattering dominates at the short waves as

$$\mu_s(\lambda) = \alpha \cdot \lambda^{-\omega} + b \cdot \lambda^{-4}, \quad (10)$$

where α and b are determined by the concentration of particles in the media, and ω is independent on the particle concentration, but depends on the particle mean size. For mediums with larger particles, a good approximation can be achieved just using a power-law decay function [49].

3 | RESULTS AND DISCUSSION

3.1 | Tissue optical transparency windows

In our study, we have obtained spectra of the healthy biological tissues. The freshly harvested rat brain cortex, cranial bone and skin samples with thicknesses of 1, 0.9 and 1 mm, respectively, were used for the ex vivo optical

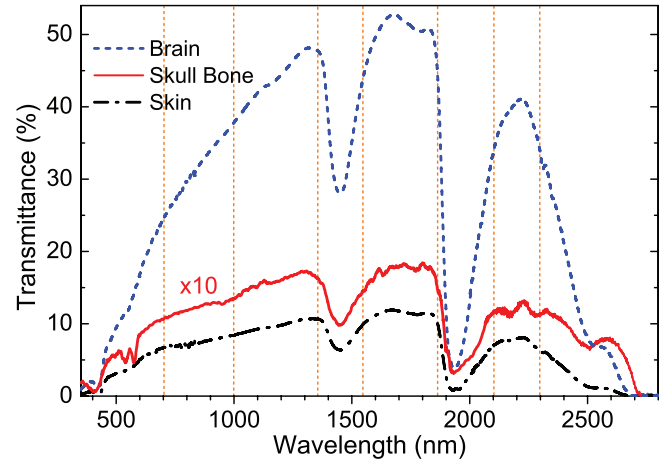


FIGURE 2 Spectra of the collimated transmittance (T_c) for the freshly harvested rat brain cortex, cranial bone and skin (thicknesses of 1, 0.9 and 1 mm, respectively)

measurements. Figure 2 shows the collimated transmittance spectra (direct light path through the sample), obtained as described in section 2: $T_c = T_d - T_s$. All the spectra clearly exhibit the dominating water absorption bands peaked at ~1450, 1950 nm and above ~2200 nm [5]. As it is known for spectral behavior of biological tissues [5, 49], scattering significantly reduces with increase in light wavelength, as predicted by Mie and Rayleigh [49]. Due to the decrease in μ_s , a distinct increase in T_c with wavelength up to ~1300 nm is observed. Considering T_c spectra, four tissue transparency windows can be identified for the investigated tissue types: ~700 to 1000 nm (NIR-I), ~1000 to 1350 nm (NIR-II), ~1550 to 1870 nm (NIR-III or SWIR) and ~2100 to 2300 nm (SWIR-II).

We have further determined the spectral dependences of μ_t using Eq. (6) (factor x_1 was taken to be 0.94 to 0.98, depending on the sample). Figure 3 shows the obtained

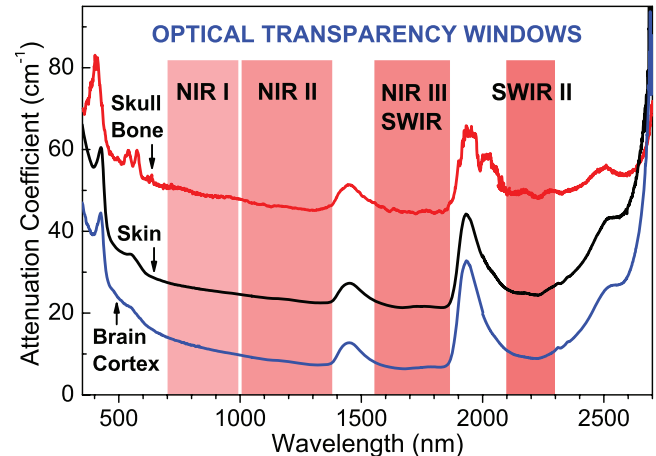


FIGURE 3 Spectra of attenuation coefficient for head tissues: brain cortex, cranial bone and skin. Four optical transparency windows are indicated: ~700 to 1000 nm (NIR-I), ~1000 to 1350 nm (NIR-II), ~1550 to 1870 nm (NIR-III or SWIR) and ~2100 to 2300 nm (SWIR-II)

spectra, providing quantitative measure for light permeability of different head tissues; these data could be of importance for the transcranial light applications. The minimum values of μ_t for the tissues determined in each optical window are given in Table 1.

Regarding the light permeability in different windows, SWIR window demonstrates the highest light penetration (the lowest μ_t) for all the as-prepared rat brain cortex, cranial bone and skin samples, the transmittance is lower in NIR-II and lowest in NIR-I and SWIR-II windows. However, there are peculiarities specific for different head tissues.

In particular, for the brain samples, light penetration in SWIR-II is a bit higher than that in NIR-I window, similar to the results reported by Shi et al. [18]. It is worth nothing that the optical properties of brain tissue have been examined previously, mostly utilizing samples from different human brain areas, such as cortex, gray or white matter, though it was done for more narrow spectral regions [17, 19–21]. All the presented data revealed strong increase in the transmittance with wavelength in NIR together with the trend that the gray matter is more transparent than the white [17, 19–21]. In case of SWIR window (at ~ 1700 nm), μ_t of the human cortex was determined to be 20 to 35 cm^{-1} [17, 21]. In our experiments, the samples were extracted from the rat brain cortex surface, and we obtained much lower μ_t of 6.5 cm^{-1} at the same wavelength. It would be natural to suggest that the value of μ_t can be affected by the way how samples are excised (eg, finely separated rat cortex surface is more transparent due to lower scattering). As a matter of fact, extinction of light by biological tissues is strongly variable: μ_t values for SWIR light have been reported to be ~ 9 to 20 cm^{-1} for mammalian muscle, fat or dura mater of spinal cord, which are known to scatter light stronger than the brain [11]. Apparently, the time delay before postmortem spectral measurements also significantly influences the attenuation values.

The skull and scalp skin have high light extinction, penetration depth for these tissues in SWIR-II are comparable to that in NIR-I (see Table 1). The reason for the observed ratio between permeability in different windows is a higher absorption in SWIR and SWIR-II ranges along with higher scattering in NIR-I and NIR-II.

It should be noted that the attenuation spectra of the human bone in the wide range from 650 to 2500 nm, reported in ref. [16], exhibit similar spectral behavior of the bone permeability, in particular, a strong absorption in

SWIR region. At ~ 1700 nm, μ_t of the human bone surface was determined to be ~ 85 cm^{-1} [16]. In our experiments, inspecting the whole thickness of the rat skull, we obtained lower μ_t of 44 cm^{-1} at the same wavelength. It should be noted that in our case we assessed a whole thickness of the rat skull, including both compact and spongy skull bones. Obviously, our attenuation values should be different from those obtained for the skull surface. In other works [13, 14, 17, 57–60], the optical extinction coefficients of mammalian bone tissues were determined in narrow spectral range (mostly for NIR) and a value of reduced attenuation μ'_t ($\mu'_t = \mu_a + \mu'_s$) was found to be ~ 10 to 30 cm^{-1} , denoting an increase in the light penetration while moving toward longer wavelengths.

Optical properties of skin were fundamentally studied in a wide spectral range [6–8], and their spectra coincide well with the spectrum presented in Figure 3, similarly defining the optical windows. For all works, where propagation of light was studied in a wide spectral range, SWIR and NIR-II regions were characterized by the lowest μ_t (~ 25 –50 cm^{-1}), providing a solid basis for various biophotonics applications in the last decade.

Generally, a disparity in light permeability for different optical windows and the characteristic spectral features are associated with the content and structure of every tissue type. The influence of the inherent tissue constituents (components) is reflected in the spectra of μ_a described below in section 3.2. Size of particles in the tissues governs the μ_s dependences, fitted by us according to the Mie and Rayleigh scattering theory (Eq. (10)) and presented in Figure 4. The dependences, in general, correspond to the spectral behavior of scattering for similar biological tissues [8, 9, 14]. Moving toward longer wavelengths in the spectral dependence of μ_s for the brain cortex and skin samples (Figure 4A,C), it first decreases abruptly from 350 to 700 nm, according to Rayleigh dependence, then, in IR region, μ_s decreases smoothly, according to Mie theory. The fitting functions are $\mu_s = 12 \cdot 450 \cdot \lambda^{-1.05} + 2 \cdot 10^{11} \cdot \lambda^{-4}$ for the brain and $\mu_s = 163 \cdot \lambda^{-0.28} + 3.4 \cdot 10^{11} \cdot \lambda^{-4}$ for the skin. In contrast, the scattering intensity for the cranial bone slowly decreases following the Mie power law, as reported by other researchers [13, 14]. The fitting function for the cranial bone is $\mu_s = 227 \cdot \lambda^{-0.23}$ (Figure 4B).

From the comparison of μ_t for all the windows, it can be stated that the SWIR window does have the maximal light permeability for all the studied tissue types. It is worth noting that tissues have lesser permeability in NIR-I,II windows, though they have been shown to be suitable for transcranial brain imaging [23–25, 34]. At the same time, it is important to note that SWIR-II window also manifests potential for the transcranial brain imaging [18], being comparable with NIR-I,II in terms of collimated/ballistic light propagation (Figures 2 and 3).

TABLE 1 Minima in the attenuation coefficient μ_t (cm^{-1}) for each optical window

Tissue	NIR-I	NIR-II	SWIR	SWIR-II
Brain cortex	10 \pm 0.5	7.4 \pm 0.4	6.5 \pm 0.3	9 \pm 0.5
Cranial bone	48 \pm 2.9	45 \pm 2.7	44 \pm 2.6	49 \pm 3.1
Skin	25 \pm 1.1	23 \pm 1.0	21 \pm 1.2	24.5 \pm 1.5

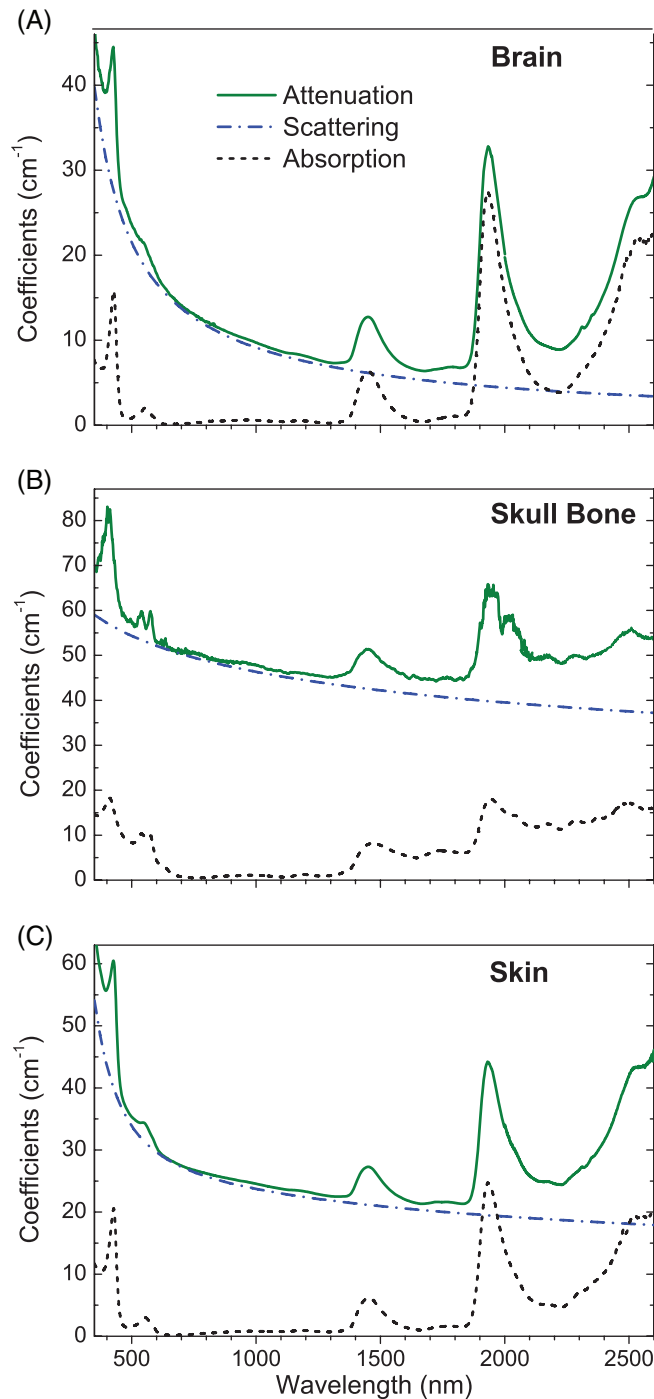


FIGURE 4 Spectral dependences of the attenuation and absorption coefficients along with fitted scattering for the freshly harvested rat brain cortex (A), skull bone (B) and skin (C)

3.2 | Manifestation of the tissue main constituents in the optical absorption spectra

The light permeability of the biological tissue in NIR and SWIR spectral regions is strongly governed by the absorption of the inherent tissue constituents, such as water, collagen, melanin, lipids and proteins. To identify the related peaks, μ_a spectra were obtained for the rat brain cortex, cranial bone and skin samples after desiccation (Figure 5), using the KM model as described in section 2.3. As noted

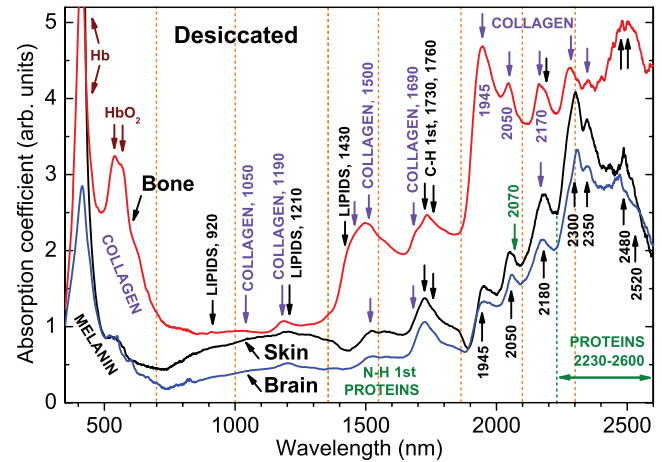


FIGURE 5 Spectral dependences of the absorption coefficient for the brain (blue), skull bone (red) and skin (black) samples after the desiccation. The major bands of the generic tissue components are marked

above, water absorption significantly determines the permeability of tissues; it has peaks around 970, 1180, 1450, 1775, 1930 and 1975 nm and the most intense bands are apparent in the spectra of the fresh tissues presented in Figure 4. The peak at ~1450 nm is referred to the first overtone of O-H stretching, the ~1930 nm peak is related to the O-H stretch/deformation combination, and the peak at ~1975 nm is attributed to the O-H second overtone [61]. The less intense absorption peaks at 970 and 1180 nm are from a vibrational overtone of the O-H bend [62]. The absorption of the skin and brain samples is comparable, while skull has less water content.

Figure 5 shows spectra of the same rat brain, cranial bone and skin samples as in Figure 4, but after the desiccation. Under such condition of low humidity, the absence of intense and spectrally broad water bands eases the identification of absorption bands of tissue components. The most distinguished absorption bands have been marked in Figure 5. It should be noted that the spectral positions for the peaks are same for both freshly harvested and desiccated samples.

Whole blood intensely absorbs light in visible and NIR ranges and strongly contributes to the absorption of most tissue constituents, though the blood is only a fraction of body volume. All head tissues have an extended blood vessel and capillary system that leads to the pronounced blood signature in the tissue absorption (Figure 4). Thus, the characteristic hemoglobin bands peaked at ~420 and ~550 nm dominate in the visible absorption spectra for all the samples. There are some disparities between soft head tissues and bone: the absorption spectra of skin and brain cortex exhibited a single absorption peak at 550 nm related to deoxy-hemoglobin (Hb), while the double-peak absorption at 540 and 575 nm from oxy-hemoglobin (HbO₂) is detected for skull bone, as also reported in the literature [13]. In addition, the absorption peak at 410 nm for the bone tissues is seen to be blue-shifted in comparison with the corresponding

peak for the soft head tissues. All this points to a higher percentage of HbO₂ in the bone samples.

A high level of HbO₂ in soft tissues was observed both *in vitro* and *in vivo* [19], and the authors assumed that this originate from the local environment of the sample during measurements or from the sample extraction method. Indeed, after the long lasting exposure to air, the soft tissue samples showed a very high level of HbO₂ indicated by the respective bands matching with the skull HbO₂ bands (Figure 5). Thus, in our case, a higher percentage of HbO₂ in the bone samples can be due to the peculiar bone pore structure (larger surface area) and constant exposure to air. As a result, the extracted bone sample is more affected by oxygen. A much lower content of HbO₂ in the soft tissue samples is apparently associated with that the samples were placed between slides immediately after excising, so the exposure to room air was minimal. Under this experimental design, measured in soft samples concentrations of hemoglobin are adequate to the *in vivo* tissue characteristics. It is known that the extinction of the biological tissues, being measured *ex vivo*, is dependent on temperature, pH or even time after extraction [11], and these external factors can affect the physiology and, correspondingly, spectroscopic data obtained from the samples.

Lipids are one of the important constituents of biological tissues, exhibiting major absorption peaks at 920, 1040, 1210, 1430, 1730, 1760 and 1900 to 2600 nm (Figure 5); they originate from overtones of the stretching vibrational mode of C-H bond [33, 43, 62–66]. The most intense peaks at 1730 and 1760 nm originate from the first overtone of C-H stretching [33, 41, 42], marked in Figure 5 as C-H 1st; the peaks at 920 and 1210 nm are associated with the second overtone of C-H stretching [33, 42]. The second combination band located between 1350 and 1500 nm (maximum at ~1430 nm), is attributed to the combination of harmonic stretching and nonstretching lipid bonds, such as bending, twisting and rocking [41, 61]. The broad band at 1900 to 2600 nm (with major peaks at 1945, 2050, 2180, 2300, 2350, 2480 and 2520 nm) is referred to C-H combinations [65, 66]. However, for fresh tissues, most of the weak bands are overlapped with water, collagen and protein bands, and in the absorption spectra, mainly primary peaks from the first overtone of C-H stretching, can be distinguished. At the same time, the lipid bands can be weakly resolved for the skull bone samples, due to the fact that the main components of bone consist of minerals as calcium hydroxyapatite (50%–70%), collagen (16%–30%), noncollagen proteins (1.5%–3%), lipids (<3%) and lesser water than in soft tissues (10%–15%) [67]. Higher lipid content results in stronger bone absorption in SWIR range if comparing with the soft tissues.

Collagen is known to be the most abundant protein in the human body and its contribution to the absorption spectra can be specifically highlighted. The optical permeability of skin and bone is substantially determined by the

absorption of collagen due to its high tissue content (less than 25% of normal skin tissue [68, 69]), despite their contribution is significantly less than that of water. In addition to the absorption band in the ultraviolet (UV) range, which is also extended to the visible one, the presence of collagen can be identified by absorption bands in NIR-SWIR region [62, 70], with peaks at around 1050, 1190, 1500, 1690, 1730, 1760, 1945, 2050, 2170, 2300 and 2350 nm [16, 41, 42, 63]. The primary collagen peaks at 1730 and 1760 nm are associated with C-H first overtone, the peak at 1190 nm corresponds to the second overtone of C-H stretching [42], while the 1500 nm peak is related to the combination of CH₂CH₂ stretching and nonstretching [41]. Furthermore, the shoulder at 1700 nm is associated with symmetric and asymmetric stretching bands from CH₂CH₂ bond, and the peak at 1690 nm comes from the first overtone of CH₃CH₃ stretching [42]. All those peaks constitute spectrally broad bands at 1350 to 1650 nm and group at 1650 to 1870 nm with the noticeable collagen peaks at 1190 and 1690 nm, which are easier to distinguish (Figure 5).

Proteins also manifest weak bands at around 1420 to 1600 and 800 to 1100 nm, which correspond to the first and second overtone of N-H stretching, respectively [65, 66]. Furthermore, spectra in Figure 5 also reveal several protein bands in SWIR region peaked at 2070 and 2230 to 2600 nm [65, 71], which are correspondingly referred to N-H and C-H combinations [66]. Other weak protein bands are overlapped with water and lipid bands and cannot be distinguished.

Herein, the skull bone spectra display more prominent broad collagen bands (1945, 2050, 2170, 2300 and 2350 nm) overlapping with the lipid ones, which correlates with the results of [14, 16]. As for skin, the collagen bands seem to dominate over the lipid ones that can be seen from the ratio of their bands around 1500 nm.

All in all, summarizing results on the optical absorptance measurements for all the head tissue samples, one can conclude that major spectral features are similar, originating from high water, lipid and collagen content. It should be noted that the lipid and collagen bands in NIR-II and SWIR ranges (ie, 1180–1220 nm and 1680–1760 nm) and several characteristic peaks of lipids and proteins in SWIR-II are easily distinguishable in the optical absorption/transmission spectra of head tissues. Absorption of different tissue constituents contributes to absorption of all tissue types in all optical windows, thereby defining window ranges and light permeability.

All tissues have the most prominent absorption peaks of water, lipids, collagen and proteins in NIR-II-SWIR-II, with no notable spectral features in visible or NIR-I (Figure 5). Availability of these peaks makes the extended SWIR region advantageous for optical spectroscopy of biological tissues [33]. Spectroscopy techniques has been applied to brain [22, 72, 73] or bone [74, 75] tissues, allowing for identification

and monitoring of tissue endogenous constituents (eg, lipids) in SWIR and SWIR-II windows [41–43]. It can be assumed that this approach can be extended to the spectral imaging, aiming at the localization and visualization of the tissue constituents in situ. For this imaging approach, the possibility to spectrally resolve bands is very important, as well as optical permeability, which can be enhanced by moving to SWIR. Furthermore, in NIR-II and extended SWIR windows, lipid or protein bands have a high ratio of absorbance against the surrounding background or close-standing bands. In particular, SWIR-II window has promises due to the existence of three peculiar close-standing not overlapping strong absorption bands of lipids (2180 nm), proteins (2170 and 2300 nm) and water.

3.3 | Light penetration depth

The total attenuation length l_t is one of the main optical parameters, which defines the spatial resolution and depth of bioimaging. Parameter l_t characterizes light propagation in turbid tissue medium and covers the coherent (ballistic) light part monitoring, being calculated using the modified Beer-Lambert law, Eq. (5). The evaluation of l_t was in the focus of recent studies targeting fields of biophotonics and medical optics [16, 18, 32], as it visualizes the dependence of tissue permeability on wavelength, providing a distinct quantification of the light penetration depth.

In the current study, l_t was calculated for rat brain cortex, cranial bone and scalp skin in the spectral range from 350 to 2700 nm using Eq. (5) (Figure 6A). The spectra indicate that l_t for all tissue types is maximal in SWIR window and comparable in NIR and SWIR-II windows. It is worth, however, noting that there are some dissimilarities between different tissues: l_t for the brain sample is slightly higher in SWIR-II than in NIR-I, while for the cranial bone and skin, there is the opposite trend. The maximal values of l_t obtained for each optical window are given in Table 2. Comparing them for all the head tissues, it can be stated that the maximal value of l_t is 3 and 6 times higher for brain than for scalp skin and cranial bone, respectively.

Using the obtained values of l_t , collimated light propagation in a continuous tissue can be evaluated for all transparency windows using the Beer-Lambert law. Curves of the fitted transmittance in Figure 6B reveal a distinct prospect for detection of the low-intensity collimated light through tissue with thickness up to centimeter for naked brain [31], and several millimeters for skin and bone. With utilization of this possibility, a successful trough-skull mouse brain imaging has been reported, exploiting NIR [23–25] and SWIR [31–33, 36] ranges. Moreover, the latest achievements on tissue clearing [76] suggest that permeability of light into tissue can be increased by application of the immersion liquid to govern tissue optical characteristics. This technique, along with choice of NIR-SWIR spectral range and a possibility of using temporary or permanent cranial windows [76], brings

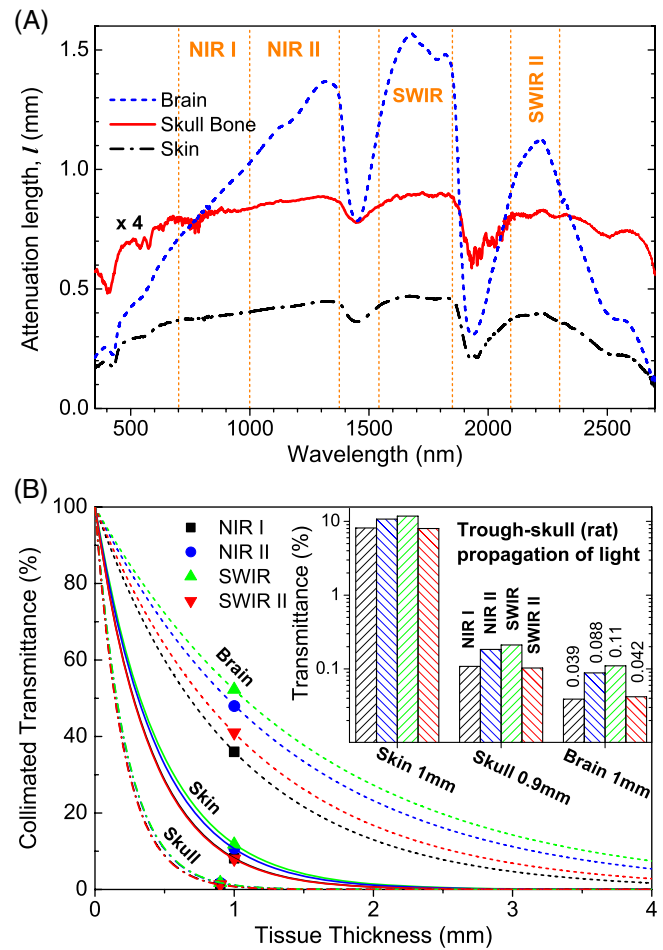


FIGURE 6 (A) Attenuation length l_t spectra and (B) fitting of the collimated transmission vs tissue thickness by the Beer-Lambert law for the freshly harvested rat brain cortex, cranial bone and skin. Inset: the estimation of light propagation through the tissue samples for four optical windows in NIR and SWIR. Passing the rat head and slice of brain, light beam remains the most intense in SWIR and NIR-II windows, while light permeability in SWIR-II and NIR-I is lesser but close to each other

great promises, paving the way to the efficient optical imaging of brain in vivo.

To visualize the obtained results for the propagation of collimated light through different head tissues, simple calculation of light extinction for the continuous rat head tissues was performed (inset in Figure 6B). After passing the head skin of ~1 mm thickness, light is attenuated ~10 times. While propagating through the 0.9 mm thick skull bone, as a result of strong scattering and absorption, light is attenuated ~50 to 80 times (depending on the spectral window) more than in the skin. Finally, when light penetrates into the brain cortex tissue, its intensity decreases by 2 to 2.8 times per 1 mm of the path, and the values of light intensity after all three types of head tissues are 0.11%, 0.088%, 0.042% and 0.039% of the initial incident light in SWIR, NIR-II, SWIR-II and NIR-I windows, respectively. Of course, these values are only evaluation data, as the considered model is rather simplified and may have some inaccuracy caused by the way how μ_t and l_t were determined (ie, difference introduced

TABLE 2 Maxima in the attenuation length l_t (mm) for each optical window

Tissue	NIR-I	NIR-II	SWIR	SWIR-II
Brain cortex	1.0 ± 0.05	1.35 ± 0.07	1.54 ± 0.08	1.11 ± 0.06
Cranial bone	0.2 ± 0.01	0.22 ± 0.01	0.23 ± 0.01	0.2 ± 0.01
Skin	0.4 ± 0.02	0.44 ± 0.02	0.47 ± 0.02	0.41 ± 0.03

by the postmortem measurements and estimation of light escaped through the sample boundaries). However, the advantages of SWIR and NIR-II windows for light penetration are clearly identified.

After comparison of data in Figures 2–3 and 4, it can be concluded that SWIR and NIR-II windows are obviously better in terms of light permeability and the SWIR window has a distinct permeability maximum for all tissue types. Light in this optical window penetrates into tissue up to 2 times deeper than light in NIR-I range.

At the same time, the newly considered SWIR-II window can also have a potential for transcranial light applications, being comparable with NIR-I,II in propagation of the collimated light (ballistic photons). Though both SWIR and SWIR-II windows have been recently applied for the through-skull brain imaging [23–25, 34], the advantage of SWIR-II is not as evident, as the light in this is attenuated similar to NIR-I (Figure 6B, inset). However, it should be noted that the light attenuation in SWIR-II range occurs more at the expense of absorption due to a decrease in light scattering with shifting toward IR wavelengths (Figure 4). In a view of high light scattering by bone tissues and considering that the reduced scattering is important to improve the imaging contrast and resolution [23, 24], it should be emphasized that the use of SWIR-II range may provide special benefits for the transcranial imaging.

It is also worth noting that the extended SWIR range may be considered for brain imaging based on the endogenous contrast originated from the distinctive spectral features of the tissue constituents in this region (eg, the existence of the close but not overlapping intense absorption bands of lipids at 2165 nm, proteins around 2300 nm and water near 2480 nm). In particular, taking into account a high lipid content of a brain tissue [77] and the reported use of SWIR and SWIR-II windows for IR spectroscopy to detect/localize lipids ex vivo [41–43] and in vivo [78–81], an approach utilizing extended SWIR region for lipid-based brain imaging can be suggested.

4 | CONCLUSIONS

The optical permeability of the rat head tissues, such as brain cortex, cranial bone and skin has been estimated, aiming to the transcranial light applications, such as brain imaging or therapy. The transmission and absorption spectral measurements were carried out in the broad spectral range from

350 to 2800 nm. Four tissue transparency windows have been identified for all considered head tissues: ~700 to 1000 nm (NIR-I), ~1000 to 1350 nm (NIR-II), ~1550 to 1870 nm (SWIR) and ~2100 to 2300 nm (SWIR-II).

Optical attenuation coefficients have been determined for all optical transparency windows of the tissues investigated here. All the optical spectra indicate the maximum tissue permeability for SWIR light, and a good transmittance in NIR, NIR-II and SWIR-II windows. While SWIR-II window was reported previously for brain, skin, muscle, adipose and organs, the distinct existence of SWIR-II for bone tissues has been shown by us for the first time, and it can be assumed that this window has a significant potential for the transcranial light applications.

Furthermore, we have assessed tissue optical absorption in all four windows, defining and describing the characteristic bands for every tissue type. The most prominent absorption band of tissue constituents have been identified in the extended SWIR range. Our data are in good agreement with values of optical coefficients of soft mammalian tissues reported elsewhere.

ACKNOWLEDGMENTS

This research was supported in part by National Natural Science Foundation of China [61525503, 61620106016, 81727804, 61722508]; National Basic Research Program of China [2015CB352005]; Guangdong Natural Science Foundation Innovation Team [2014A030312008]; Shenzhen Basic Research Project [JCYJ20150930104948169, JCYJ20160328144746940, GJHZ20160226202139185, JCYJ20170412105003520].

Conflicts of interest

The authors have no conflicts of interest to declare.

AUTHOR BIOGRAPHIES

Please see Supporting Information online.

ORCID

Sergii Golovynskyi  <https://orcid.org/0000-0002-1864-976X>

Iuliia Golovynska  <https://orcid.org/0000-0003-3916-6588>

Ludmila I. Stepanova  <https://orcid.org/0000-0002-8833-9409>

Oleksandr I. Datsenko  <https://orcid.org/0000-0002-4461-1925>

Junle Qu  <https://orcid.org/0000-0001-7833-4711>

Tymish Y. Ohulchanskyy  <https://orcid.org/0000-0002-7051-6534>

REFERENCES

- [1] P. N. Prasad, *Introduction to Biophotonics*, Wiley-Interscience, Hoboken, NJ 2003.
- [2] L. Teodori, A. Crupi, A. Costa, A. Diaspro, S. Melzer, A. Tarnok, *J. Biophotonics* 2017, 10, 24.

- [3] Y. Li, S. J. Montague, A. Brüstle, X. He, C. Gillespie, K. Gaus, E. E. Gardiner, W. M. Lee, *J. Biophotonics* **2018**, *11*, e201700341.
- [4] J. Titus, H. Ghimire, E. Viennois, D. Merlin, A. G. Unil Perera, *J. Biophotonics* **2018**, *11*, e201700057.
- [5] S. L. Jacques, *Phys. Med. Biol.* **2013**, *58*, R37.
- [6] J. A. Parrish, *J. Invest. Dermatol.* **1981**, *77*, 45.
- [7] R. R. Anderson, J. A. Parrish, Optical Properties of Human Skin. In: Regan J.D., Parrish J.A. (eds) *The Science of Photomedicine. Photobiology*. Springer, Boston **1982**, 147. https://doi.org/10.1007/978-1-4684-8312-3_6.
- [8] A. N. Bashkatov, E. A. Genina, V. I. Kochubey, V. V. Tuchin, *J. Phys. D. Appl. Phys.* **2005**, *38*, 2543.
- [9] A. N. Bashkatov, E. A. Genina, V. I. Kochubey, V. V. Tuchin, *Opt. Spectrosc.* **2005**, *99*, 836.
- [10] A. N. Bashkatov, E. A. Genina, V. V. Tuchin, *J. Innov. Opt. Health Sci.* **2011**, *4*, 9.
- [11] S. A. Filatova, I. A. Shcherbakov, V. B. Tsvetkov, *J. Biomed. Opt.* **2017**, *22*, 35009.
- [12] P. Taroni, A. Pifferi, A. Torricelli, D. Comelli, R. Cubeddu, *Photochem. Photobiol. Sci.* **2003**, *2*, 124.
- [13] H. Soleimanzad, H. Gurden, F. Pain, *J. Biomed. Opt.* **2017**, *22*, 010503.
- [14] V. V. Tuchin, A. N. Bashkatov, E. A. Genina, V. I. Kochubey, V. V. Tuchin, *Saratov Fall Meeting 2005: Optical Technologies in Biophysics and Medicine VII*, Proc. of SPIE Vol. 6163, 616310 (SPIE, Bellingham, Washington, USA), **2006**, p. 616310. <https://doi.org/10.1117/12.697305>.
- [15] A. H. Barnett, J. P. Culver, A. G. Sorensen, A. Dale, D. A. Boas, *Appl. Opt.* **2003**, *42*, 3095.
- [16] D. C. Sordillo, L. A. Sordillo, P. P. Sordillo, L. Shi, R. R. Alfano, *J. Biomed. Opt.* **2017**, *22*, 45002.
- [17] F. Bevilacqua, D. Piguet, P. Marquet, J. D. Gross, B. J. Tromberg, C. Depeursinge, *Appl. Opt.* **1999**, *38*, 4939.
- [18] L. Shi, L. A. Sordillo, A. Rodriguez-Contreras, R. Alfano, *J. Biophotonics* **2016**, *9*, 38.
- [19] S. C. Gebhart, W. C. Lin, A. Mahadevan-Jansen, *Phys. Med. Biol.* **2006**, *51*, 2011.
- [20] A. N. Yaroslavsky, P. C. Schulze, I. V. Yaroslavsky, R. Schober, F. Ulrich, H. J. Schwarzmair, *Phys. Med. Biol.* **2002**, *47*, 2059.
- [21] N. G. Horton, K. Wang, D. Kobat, C. G. Clark, F. W. Wise, C. B. Schaffer, C. Xu, *Nat. Photonics* **2013**, *7*, 205.
- [22] S. J. Madsen, *Optical Methods and Instrumentation in Brain Imaging and Therapy*, Springer, New York **2013**.
- [23] G. Hong, S. Diao, J. Chang, A. L. Antaris, C. Chen, B. Zhang, S. Zhao, D. N. Atochin, P. L. Huang, K. I. Andreasson, C. J. Kuo, H. Dai, *Nat. Photonics* **2014**, *8*, 723.
- [24] Y. Tsukasaki, M. Morimatsu, G. Nishimura, T. Sakata, H. Yasuda, A. Komatsuzaki, T. M. Watanabe, T. Jin, *RSC Adv.* **2014**, *4*, 41164.
- [25] J.-H. Park, W. Sun, M. Cui, *PNAS* **2015**, *112*, 9236.
- [26] L. Shi, E. J. Galvez, R. R. Alfano, *Sci. Rep.* **2016**, *6*, 37714.
- [27] G. Chen, J. Shen, T. Y. Ohulchanskyy, N. J. Patel, A. Kutikov, Z. Li, J. Song, R. K. Pandey, H. Agren, P. N. Prasad, G. Han, *ACS Nano* **2012**, *6*, 8280.
- [28] M. Nyk, R. Kumar, T. Y. Ohulchanskyy, E. J. Bergey, P. N. Prasad, *Nano Lett.* **2008**, *8*, 3834.
- [29] N. S. James, T. Y. Ohulchanskyy, Y. Chen, P. Joshi, X. Zheng, L. N. Goswami, R. K. Pandey, *Theranostics* **2013**, *3*, 703.
- [30] A. M. Smith, M. C. Mancini, S. Nie, *Nat. Nanotechnol.* **2009**, *4*, 710.
- [31] L. A. Sordillo, L. Lindwasser, Y. Budansky, P. Leproux, R. R. Alfano, *J. Biomed. Opt.* **2015**, *20*, 030501.
- [32] L. A. Sordillo, Y. Pu, S. Pratavieira, Y. Budansky, R. R. Alfano, *J. Biomed. Opt.* **2014**, *19*, 056004.
- [33] R. H. Wilson, K. P. Nadeau, F. B. Jaworski, B. J. Tromberg, A. J. Durkin, *J. Biomed. Opt.* **2015**, *20*, 030901.
- [34] E. Hemmer, A. Benayas, F. Légaré, F. Vetrone, *Nanoscale Horiz.* **2016**, *1*, 168.
- [35] D. Franke, D. K. Harris, O. Chen, O. T. Bruns, J. A. Carr, M. W. B. Wilson, M. G. Bawendi, *Nat. Commun.* **2016**, *7*, 12749.
- [36] M. Zevon, V. Ganapathy, H. Kantamneni, M. Mingozzi, P. Kim, D. Adler, Y. Sheng, M. C. Tan, M. Pierce, R. E. Riman, C. M. Roth, P. V. Moghe, *Small* **2015**, *11*, 6347.
- [37] H. Wook Shin, S. Jun Lee, D. Gun Kim, M.-H. Bae, J. Heo, K. Jin Choi, W. Jun Choi, J.-W. Choe, J. Cheol Shin, *Sci. Rep.* **2015**, *5*, 10764.
- [38] S. Golovynskyi, O. I. Datsenko, L. Seravalli, G. Trevisi, P. Frigeri, I. S. Babichuk, I. Golovynska, J. Qu, *Nanoscale Res. Lett.* **2018**, *13*, 103.
- [39] S. Golovynskyi, L. Seravalli, O. Datsenko, G. Trevisi, P. Frigeri, E. Gombia, I. Golovynska, S. V. Kondratenko, J. Qu, T. Y. Ohulchanskyy, *Nanoscale Res. Lett.* **2017**, *12*, 335.
- [40] J. Wu, S. M. Chen, A. Seeds, H. Y. Liu, *J. Phys. D. Appl. Phys.* **2015**, *48*, 363001.
- [41] P. Wang, H. W. Wang, M. Sturek, J. X. Cheng, *J. Biophotonics* **2012**, *5*, 25.
- [42] P. Wang, P. Wang, H. W. Wang, J. X. Cheng, *J. Biomed. Opt.* **2012**, *17*, 96010.
- [43] J. Wang, Y. J. Geng, B. Guo, T. Klima, B. N. Lal, J. T. Willerson, W. Casscells, *J. Am. Coll. Cardiol.* **2002**, *39*, 1305.
- [44] P. Parsa, S. L. Jacques, N. S. Nishioka, *Appl. Opt.* **1989**, *28*, 2325.
- [45] A. P. Craig, M. Jain, G. Wicks, T. Golding, K. Hossain, K. McEwan, C. Howle, B. Percy, A. R. J. Marshall, *Appl. Phys. Lett.* **2015**, *106*, 201103.
- [46] K. M. Yoo, R. R. Alfano, *Opt. Lett.* **1990**, *15*, 320.
- [47] K. M. Yoo, R. R. Alfano, *Opt. Lett.* **1990**, *15*, 276.
- [48] K. M. Yoo, F. Liu, R. R. Alfano, *Phys. Rev. Lett.* **1990**, *64*, 2647.
- [49] J. M. Schmitt, G. Kumar, *Appl. Opt.* **1998**, *37*, 2788.
- [50] M. Cope, D. T. Delpy, E. O. Reynolds, S. Wray, J. Wyatt, P. van der Zee, *Adv. Exp. Med. Biol.* **1988**, *222*, 183.
- [51] D. T. Delpy, M. Cope, P. van der Zee, S. Arridge, S. Wray, J. Wyatt, *Phys. Med. Biol.* **1988**, *33*, 1433.
- [52] H. Heusmann, J. G. Koelzer, G. Mitic, *J. Biomed. Opt.* **1996**, *1*, 425.
- [53] G. Yona, N. Meitav, I. Kahn, S. Shoham, *eNeuro* **2016**, *3*, 0059.
- [54] W. F. Cheong, S. A. Prahl, A. J. Welch, *IEEE J. Quantum. Electron.* **1990**, *26*, 2166.
- [55] S. N. Thennadil, *J. Opt. Soc. Amer. A* **2008**, *25*, 1480. <https://doi.org/10.1364/josaa.25.001480>.
- [56] C. P. Sabino, A. M. Deana, T. M. Yoshimura, D. F. T. da Silva, C. M. França, M. R. Hamblin, M. S. Ribeiro, *J. Photochem. Photobiol. B Biol.* **2016**, *160*, 72.
- [57] A. Pifferi, A. Torricelli, P. Taroni, A. Bassi, E. Chikoidze, E. Giambattistelli, R. Cubeddu, *J. Biomed. Opt.* **2004**, *9*, 474.
- [58] N. Ugryumova, S. J. Matcher, D. P. Attenburrow, *Phys. Med. Biol.* **2004**, *49*, 469.
- [59] S. Tauber, R. Baumgartner, K. Schorn, W. Beyer, *Lasers Surg. Med.* **2001**, *28*, 18.
- [60] M. Firbank, M. Hiraoka, M. Essenpreis, D. T. Delpy, *Phys. Med. Biol.* **1993**, *38*, 503.
- [61] J. Workman, L. Weyer, *Practical Guide to Interpretive Near-Infrared Spectroscopy*, CRC Press, Boca Raton, FL **2008**.
- [62] T. J. Allen, A. Hall, A. P. Dhillon, J. S. Owen, P. C. Beard, *J. Biomed. Opt.* **2012**, *17*, 061209.
- [63] J. D. Caplan, S. Waxman, R. W. Nesto, J. E. Muller, *J. Am. Coll. Cardiol.* **2006**, *47*, C92.
- [64] F. E. Barton, D. S. Himmelsbach, J. H. Duckworth, M. J. Smith, *Appl. Spectrosc.* **1992**, *46*, 420.
- [65] R. Marbach, H. M. Heise, *Appl. Opt.* **1995**, *34*, 610.
- [66] B. G. Osborne, *Encyclopedia of Analytical Chemistry*. In: Robert A. Meyers (editor) *Encyclopedia of Analytical Chemistry: Applications, Theory and Instrumentation* (John Wiley & Sons, Chichester). **2006**, p. 1. <https://doi.org/10.1002/9780470027318.a1018>.
- [67] B. Clarke, *Clin. J. Am. Soc. Nephrol.* **2008**, *3*, S131.
- [68] J. Heino, *Bioessays* **2007**, *29*, 1001.
- [69] S. Ricard-Blum, *Cold Spring Harb. Perspect. Biol.* **2011**, *3*, a004978. <https://doi.org/10.1101/cshperspect.a004978>.
- [70] Y. Pu, W. Wang, G. Tang, R. R. Alfano, *J. Biomed. Opt.* **2010**, *15*, 047008.
- [71] C. Kalaitzidis, S. J. M. Caporn, M. E. J. Cutler, *Water Air Soil Pollut.* **2008**, *194*, 57.
- [72] H. E. D'Arceuil, M. P. Hotakainen, C. Liu, G. Themelis, A. J. de Crespigny, M. A. Franceschini, *J. Biomed. Opt.* **2005**, *10*, 011011.
- [73] J. R. Mahoney, R. Holtzer, M. Izzetoglu, V. Zemon, J. Verghese, G. Allali, *Brain Res.* **2016**, *1633*, 126.
- [74] I. O. Afara, I. Prasad, R. Crawford, Y. Xiao, A. Oloyede, *Bone* **2013**, *53*, 350.
- [75] B. R. Klyen, L. Scolaro, T. Shavlakadze, M. D. Grounds, D. D. Sampson, *Biomed. Opt. Express* **2014**, *5*, 1217.
- [76] Y. J. Zhao, T. T. Yu, C. Zhang, Z. Li, Q. M. Luo, T. H. Xu, D. Zhu, *LSA* **2018**, *7*, 17153.
- [77] H. McIlwain, H. S. Bachelard, *Biochemistry and the Central Nervous System*, Churchill Livingstone, Edinburgh, NY **1985**.

- [78] R. D. Madder, M. Husaini, A. T. Davis, S. VanOosterhout, M. Khan, D. Wohns, R. F. McNamara, K. Wolschleger, J. Gribar, J. S. Collins, M. Jacoby, J. M. Decker, M. Hendricks, S. T. Sum, S. Madden, J. H. Ware, J. E. Muller, *Eur. Heart J. Cardiovasc. Imaging* **2016**, *17*, 393. <https://doi.org/10.1093/ehjci/jev340>.
- [79] R. D. Madder, M. Khan, M. Husaini, M. Chi, S. Dionne, S. Van Oosterhout, A. Borgman, J. S. Collins, M. Jacoby, *Circ. Cardiovasc. Imaging* **2016**, *9*, e003576. <https://doi.org/10.1161/CIRCIMAGING.115.003576>.
- [80] B. A. Danek, A. Karatasakis, J. Karacsonyi, A. Alame, P. Kalsaria, E. Resendes, B. V. Rangan, S. Banerjee, E. S. Brilakis, *Contin. Cardiol. Educ.* **2016**, *2*, 89. <https://doi.org/10.1002/cce2.23>.
- [81] B. A. Danek, A. Karatasakis, J. Karacsonyi, A. Alame, E. Resendes, P. Kalsaria, P. J. Nguyen-Trong, B. V. Rangan, M. Roesle,

S. Abdullah, S. Banerjee, E. S. Brilakis, *Cardiovasc. Revasc. Med.* **2017**, *18*, 177.

How to cite this article: Golovynskyi S, Golovynska I, Stepanova LI, et al. Optical windows for head tissues in near-infrared and short-wave infrared regions: Approaching transcranial light applications. *J. Biophotonics*. 2018;11:e201800141. <https://doi.org/10.1002/jbio.201800141>